**Granular Shape Memory Ceramic Packings**

Hang Z. Yu[a,†], Mostafa Hassani-Gangaraj [a], Zehui Du[b], Chee Lip Gan [b,c], and Christopher A. Schuh[a,*]

a Department of Materials Science and Engineering, Massachusetts Institute of Technology, Cambridge, MA 02139, USA

b Temasek Laboratories, Nanyang Technological University, 637553, Singapore

c School of Materials Science and Engineering, Nanyang Technological University, 639798, Singapore

[*] Corresponding author: schuh@mit.edu

[†] Current address: Department of Materials Science and Engineering, Virginia Tech, Blacksburg, VA 24061, USA

**Although bulk shape memory ceramics (SMCs) are brittle, in particulate form they exhibit large recoverable strains in both shape memory and superelastic modes. Here, we investigate the fundamentals of mechanically- and thermally-triggered martensitic transformation of granular SMC packings. Specifically, $(ZrO_2)_{1-x}$-$(CeO_2)_x$ is studied in three different composition regimes. In the shape memory regime (below the martensite finish temperature), confined uniaxial compression leads to martensite re-orientation in the granular SMC packing, with the peak intensity of preferred crystallographic orientation increasing with external loading. In the intermediate regime (between austenite start and martensite start temperatures), confined uniaxial compression leads to irreversible martensitic transformation with the transformed volume increasing with external loading. This provides direct evidence of stress-induced martensitic transformation in granular SMCs. In the superelastic regime (above the austenite finish temperature), confined uniaxial compression leads to forward (during loading) and reverse (during unloading) martensitic transformation, manifesting in a large hysteresis loop in each load-unload cycle with remarkably high energy dissipation density. Based on finite element modeling of SMC particles in contact, we explore the martensitic transformation under non-uniform Hertzian stresses, which in turn provides insight on the experimental results.**

Keywords: Shape memory; granular materials; zirconia; martensitic transformation; superelasticity

## 1 Introduction

Shape memory alloys exhibit two unique properties, namely the shape memory and superelastic effects, owing to a reversible martensitic transformation between two different crystallographic phases [1-10]. The forward martensitic transformation is characterized by martensite start and finish temperatures $M_s$ and $M_f$, and the reverse transformation by austenite start and finish temperatures $A_s$ and $A_f$. In the shape memory regime ($T < M_f$), the material is in the martensite phase and likely exhibits a variety of differently-oriented martensite variants, or twins; external loading leads to deformation by reorientation of the martensite variants to those that best accommodate the applied strain, with an associated shape change. Subsequent heating reverts the 'detwinned' martensite to austenite. Upon cooling, austenite transforms back to twinned martensite without a shape change due to self-accommodation [11]. In the superelastic regime $(T > A_f)$, the alloys are originally in the austenite state, and external loading leads to martensitic transformation. Upon unloading, the martensite transforms back to austenite. The martensitic phase transformation results in shear strains at the level of the crystal lattice [2, 12] which can be realized up to the macroscopic scale; a remarkably high recoverable strain (as high as ~10%) can be obtained in either the thermally- or stress-activated cases.

With the capability of reversibly transforming between tetragonal and monoclinic phases, zirconia-based ceramics [6, 12-19] represent a unique family of shape memory materials. Compared to conventional shape memory metal alloys [20, 21], zirconia-based SMCs have a much higher transformation stress, a much larger hysteresis in a load-unload cycle, and a much wider range of tunable transformation temperatures, from room temperature to 1200 °C [14, 15, 22, 23]. These properties render SMCs ideal for a wide variety of emerging applications that are unaddressable by shape memory metals, such as ultra-high energy dissipation and high-temperature actuation.

As intrinsically brittle ceramics, SMCs are not likely to survive the transformation intact if they are large and polycrystalline, because the transformation strain is far beyond the elastic limit of the lattice. This is a key challenge with these materials. Practical SMCs are therefore most likely to involve small specimen length scales and few grains [6, 24, 25], so that when the transformation happens it is unconstrained and the transformation mismatch is accommodated at free surfaces. Lai *et al.* [6] first showed that in small zirconia micropillars with very few grains

(i.e., oligocrystals or single crystals), the mismatch stresses associated with the transformation could be relieved at the pillar surfaces, permitting recoverable strains as high as ~7-8%. In superelastic cycling experiments, they demonstrated energy dissipation on the order of 100 MJ/m$^3$, two to three orders of magnitude higher than that seen in shape memory metal alloys.

With the requirement of fine specimen size scales and few grains, approaches to scaling up SMCs for bulk applications are limited. One clear approach is to use SMCs in a granular form where every individual granular particle is a fine, oligocrystalline "specimen" of SMC. An aggregation of such granules could present an effective approach to bulk-level applications, such as high-energy dissipation and vibration damping. For example, high-energy dissipation armor may comprise an encapsulated granular SMC packing, or vibration-damping devices may incorporate such a packing between more rigid vibrating surfaces [26-29]. In these cases, the input mechanical energy would be converted to heat not only through friction amongst the particles as in conventional granular packings, but also through reversible, stress-induced martensitic transformation in individual particles when the critical transformation stress state is reached, as recently seen in cyclic compression of individual micro-scale superelastic particles [30]. This application would also inherently mitigate concerns about fracture; in contrast to the sensing and actuation applications typically targeted for shape memory materials [31-36], where fracture is detrimental, fracture could be beneficial for granular SMC-based energy dissipation devices, because fracture itself releases strain energy [37, 38]. Fracture indeed would only serve to reduce the SMC particles' size, which in principle should enhance their superelastic properties on subsequent cycles.

The goal of this paper is to present the first systematic exploration of the mechanics and phase transformation behavior of granular SMCs under confined loading. Specifically, we study the mechanical and thermal responses of granular $(ZrO_2)_{1-x}$-$(CeO_2)_x$ in three different compositions designed to access three distinct behavioral regimes (see Figure 1(a)) including the conventional shape memory and superelastic regimes, as well as an intermediate regime that provides direct quantitative evidence for stress-induced martensitic transformation in SMC packings.

## 2 Experimental procedures

The $(ZrO_2)_{1-x}(CeO_2)_x$–based SMCs are synthesized by chemical co-precipitation from two dissolved salts, $Ce(NO_3)_3·6H_2O$ and $ZrOCl_2·8H_2O$, with ammonium hydroxide, followed by

washing, filtration, drying, calcination, and crystallization at 1500 °C. The ceria atomic concentration $x$ was controlled through the weight ratio of the two precursor salts as in [6, 39]. By tuning the atomic concentration of ceria, we are able to investigate thermal and mechanical responses of SMCs in different regimes:

- *The shape memory regime ($T < M_f$).* In this regime, the SMC is stable in the monoclinic phase (i.e. martensite); external loading may result in detwinning and martensite reorientation, but not phase transformation. For powders with $x = 10\%$ in $(ZrO_2)_{1-x}$-$(CeO_2)_x$, the transformation temperatures have been measured using differential scanning calorimetry (DSC), with the martensite finish temperature $M_f \sim 150$ °C, martensite start temperature $M_s \sim 210$ °C, austenite start temperature $A_s \sim 380$ °C, and austenite finish temperature $A_f \sim 430$ °C. Since the martensite finish temperature is above room temperature, this composition produces a material in the shape memory regime at room temperature.

- *The intermediate regime ($M_s<T<A_s$).* In this regime, the SMC is metastable in the tetragonal phase (i.e. austenite). It transforms to the monoclinic phase when the applied stress reaches a critical value, but will not transform back to the tetragonal phase as the applied stress is removed. For powders with $x = 12\%$ in $(ZrO_2)_{1-x}$-$(CeO_2)_x$, the as-prepared powders are already in the tetragonal phase from X-ray diffraction analysis. No martensitic transformation is detected upon cooling to -170 °C in DSC, which may be caused by kinetic constraints for martensite nucleation at low temperatures. However, from X-ray diffraction analysis, we confirm that stress causes martensitic transformation in the $(ZrO_2)_{0.88}$-$(CeO_2)_{0.12}$ powders at room temperature, which remain in the martensite state as the stress is removed. These will be shown in detail in Section 4. Therefore, this composition produces a material in the intermediate regime at room temperature, featuring metastability of the martensitic transformation [40]. The work by Chen and co-workers [41-42] also shows that $(ZrO_2)_{0.88}$-$(CeO_2)_{0.12}$ with a similar grain size falls in the intermediate regime.

- *The superelastic regime ($T> A_f$).* In this regime, the SMC is stable in the tetragonal phase (i.e. austenite). It transforms to the monoclinic phase when the applied stress reaches a critical value and transforms back as the applied stress is removed. For $x = 15\%$ in $(ZrO_2)_{1-x}$-$(CeO_2)_x$ , the materials are in the tetragonal phase at room temperature. No martensitic transformation is found by cooling to -170 °C in DSC test, and no irreversible martensitic transformation is found

by applying stresses at room temperature. Therefore, this composition produces a material in the superelastic regime at room temperature.

The relationships between transformation temperatures and composition are summarized in Figure 1(b) for the three cases in this study. After the powders with controlled composition are synthesized, they are coarsely ground using a mortar and pestle and then finely ground using a high energy ball mill (Retsch Emax). After coarse grinding, the particle size is mostly (~ 70%) in the range of 40-60 µm based on scanning electron microscopy images; individual particles often consist of multiple grains, with the grain size ranging from 3 to 10 µm. Fine grinding further reduces the particle size to 3 µm or below, as characterized using light scattering particle size analysis (Horiba LA 950). The increase in grain size by annealing and the decrease of particle size by grinding significantly reduce the number of grain boundaries and triple junctions in each SMC particle, which is helpful to promote fine, oligocrystalline SMC particles.

The mechanical behavior of granular SMCs is measured through powder-die compaction using a steel die and an Instron mechanical testing system. The displacement of the compact is measured using an extensometer between the punch and die (diameter of 6 mm) and corrected for apparatus compliance in between the extensometer attachment points by testing with an empty die. All the compaction tests are performed at room temperature, so after mechanical cycling, the initially loose powders generally form weakly bonded compacts that must be handled gently. As a control experiment, similar mechanical tests are performed for fully stabilized zirconia powders in the cubic phase with 8 mol% $Y_2O_3$ (from Sigma-Aldrich), which are not capable of any transformation.

Thermally induced phase transformations are characterized using a differential scanning calorimeter (DSC; model TGA/DSC1 from Mettler Toledo) under flowing argon cover gas, in which the sample is heated and cooled between room temperature and 500°C at a rate of 10°C/min. X-ray diffraction (XRD; X'Pert[3] from Panalytical) is used to characterize the as-prepared powders as well as the SMC packings after mechanical and thermal treatment. We adopt the standard two-theta scan method to analyze the phase and texture, in which the granular packings are first mounted onto a sample holder, and then the holder is mounted onto the sample stage inside the diffractometer.

## 3 Shape memory regime: $T < M_f$

### 3.1 Stress-induced martensite reorientation

We first study the mechanical and thermal responses of granular SMC packings in the shape memory regime ($T < M_f$) by synthesizing $(ZrO_2)_{1-x}$-$(CeO_2)_x$ with cerium atomic concentration $x$ =10%. For this composition, the martensite finish temperature $M_f$ is above 300 K, so the as-synthesized $(ZrO_2)_{0.9}$-$(CeO_2)_{0.1}$ particles are in the shape memory regime at 300 K.

Confined uniaxial compression with an average axial stress of 880 MPa is applied to the $(ZrO_2)_{0.9}$-$(CeO_2)_{0.1}$ particles in the powder-die compaction mode (Steps $1_{SM}$ and $2_{SM}$ in Figure 1 (a)). Here, the average axial stress refers to the stress on the uniaxial die, which can be much lower than the local contact stresses in any given powder particle. Confined compression converts the loose powders to a granular packing consisting of weakly bonded particles. The load-displacement curves for $(ZrO_2)_{0.9}$-$(CeO_2)_{0.1}$ powders show typical behavior of non-transforming ceramic powders, with much lower energy dissipation in each load-unload cycle than the transforming superelastic ceramic powders (Figure 9, Section 5).

X-ray diffraction patterns of as-prepared loose powders and the granular packing are compared in Figure 2 (a). The as-prepared loose powders are in the monoclinic phase, featuring two conspicuous peaks associated with the $(\bar{1}11)$ and $(111)$ planes at ~ 28° and 31° in the two-theta scan, respectively. All of the remaining peaks can also be indexed with monoclinic reflections in this case. After compression, the granular packing remains in the monoclinic phase, but there is a significant change in the ratio of $(111)$ to $(\bar{1}11)$ peak intensities; compaction has reversed the relative intensities of these two peaks. The ratio seen in the loose powders, where the $(\bar{1}11)$ peak has the maximum intensity, is what is expected for a random texture [43]. The prominence of the $(111)$ peak after compaction is a signature of texture evolution.

Figure 2 (b) shows that the ratio of $(111)$ to $(\bar{1}11)$ peak intensities increases monotonically as the average axial compaction stress rises. Because the strains achieved in compaction of the present powders are small and zirconia-based ceramics are not very malleable, the observed texture change is not likely caused by plasticity. Furthermore, the compaction tests are all performed at room temperature, where recrystallization does not occur and thus cannot explain the texture development. Instead, we believe the texture development signaled by Figure 2 as

well as its strong dependence on the magnitude of external loading suggests martensite reorientation [42, 44-47] in martensitic particles during confined uniaxial compression. Such a response is the expected one for a shape memory material loaded in the shape memory regime of Figure 1(a), and seems to be the only plausible texture evolution mechanism in the present SMC packing.

### 3.2 Thermally-induced transformations

If the compaction experiment described above indeed causes martensite reorientation at ambient temperature, then it should be reversible by thermal cycling into the austenite range and back without applied stress, following Steps $3_{SM}$ and $4_{SM}$ in Figure 1(a). We therefore characterize the heat flow of a granular packing (compacted at 880 MPa) using DSC, and compare it with uncompacted, loose powders of the same composition and weight.

Figures 3 and 4 show that both compacted and uncompacted powders transform from monoclinic to tetragonal phase during heating and revert upon cooling to room temperature. However, the shapes of the DSC curves are clearly different in the two cases. For the granular packing, instead of a single, well-defined, endothermic peak, there is a long and significant exothermic process before the reverse martensitic transformation (Figure 3); we attribute this to stress relaxation and the consequent release of strain energy, which is previously stored during confined uniaxial compression. At a temperature above $A_f$ ~430 ℃, the packing transforms to the tetragonal phase.

During cooling (Figure 4), the packing remains in the tetragonal phase until the temperature decreases below $M_S$ ~210 ℃, and then transforms back to the monoclinic phase. The reverse transformation takes place in the absence of applied load in the DSC, and thus can occur in a self-accommodating fashion; the resultant monoclinic packing has lost most of its texture. This can be seen by comparing the XRD patterns for the loose powders and the granular packing before and after the DSC cycling: the high ratio of the (111) to the $(\bar{1}11)$ peak intensities in the packing (Figure 3, upper) significantly decreases after the DSC cycling (Figure 4, upper), suggesting a loss of the texture.

To summarize, the as-synthesized $(ZrO_2)_{0.9}$-$(CeO_2)_{0.1}$ particles are in the monoclinic phase at room temperature, and exhibit a random texture before compression. External loading leads to

7

martensite reorientation and texture development in the granular SMC packing, which, in turn, largely disappears after stress-free DSC cycling that involves reverse and forward martensitic transformations. These phenomena observed here in granular SMC packings are consistent with the expectations for shape memory materials in the shape memory regime; external loading leads to detwinning [48] and martensite re-orientation and the subsequent stress-free heating-cooling cycle results in twinned martensites without directional bias. More direct evidence for the martensitic transformation can be obtained in SMC particles that are designed to metastably remain in a transformed condition after transformation, i.e., in the intermediate regime, as discussed in the next section.

## 4 Intermediate regime: $M_s < T < A_s$.

### 4.1 Direct evidence for stress-induced martensitic transformation

In the intermediate regime, the as-synthesized materials are in the tetragonal phase because $M_s$ lies below room temperature. However, $A_s$ lies above room temperature in this regime, meaning that the particles, once transformed to the monoclinic phase at room temperature by external stimulus (e.g. stress), will remain in the monoclinic phase even when the external stimulus is removed. Therefore, in the intermediate regime, the stress-induced martensitic transformation is irreversible, allowing for quantitative *ex situ* characterization of the transformation.

Similar to Section 3, confined uniaxial compression with an average axial stress of 880 MPa is applied to the $(ZrO_2)_{0.88}$-$(CeO_2)_{0.12}$ particles in the powder-die compaction mode (Steps $1_I$ and $2_I$ in Figure 1 (a)). This converts the loose powders to a granular packing consisting of weakly bonded particles. The load-displacement curves for $(ZrO_2)_{0.88}$-$(CeO_2)_{0.12}$ powders for the initial loading resemble the first curve for the superelastic powders (Figure 9, Section 5). After the first loading, the load-displacement curves show typical behavior of non-transforming ceramic powders, with much lower energy dissipation in each load-unload cycle than the transforming superelastic ceramic powders.

Figure 5 shows representative XRD patterns of SMCs in the intermediate regime, with ceria content $x = 12\%$. The as-prepared $(ZrO_2)_{0.88}$-$(CeO_2)_{0.12}$ SMC particles are mostly in the tetragonal phase at room temperature, featuring a strong (101) tetragonal diffraction peak at ~29.96° in the XRD pattern. Since these powders are in the intermediate regime and are capable

of retaining monoclinic martensite phase at room temperature, there are signatures of that phase in the pattern as well. After uniaxial compression, the majority of the granular packing is in the monoclinic phase with characteristic $(\bar{1}11)$ and $(111)$ peaks labelled. The data in Figure 5 thus provides the first direct evidence for stress-induced transformation in granular SMCs under confined uniaxial compression.

This irreversible transformation allows us to quantitatively characterize the relationship between transformed volume and external loading. Figure 6 plots the volume fraction of the monoclinic phase as a function of the average axial stress. The as-processed powders already contain a small fraction of the monoclinic phase; upon compression, further transformation occurs. It can be seen that even under a small load with an average axial stress of 70 MPa, a significant volume fraction of additional tetragonal phase transforms to the monoclinic phase, and as the load increases, greater conversion is observed. This is quite different from the case of uniaxial compression of SMC pillars, in which martensitic transformation does not occur until a high critical stress (often on the order of 1 GPa) is reached [6, 48]. The behavior observed in granular SMC packings originates from the highly non-uniform stress distribution in powder-die compaction; the concentration of stresses and strains near particle-particle contacts [50-51] produces local transformation that expands through an increasing volume as the average axial stress increases.

Another interesting phenomenon in Figure 6 is that when the average axial stress exceeds 500-600 MPa, the monoclinic volume fraction asymptotically approaches an apparent maximum value. The limit of the transformed volume fraction is apparently around 75%. Assuming that the original ~35% or so of the martensite phase in the as-processed powder does not contribute mechanically, the asymptotic level of additional transformation caused by external loading is estimated around 40%. The origin of this plateau of the transformation volume (or the limit of transformation) will be discussed at greater length in a later section.

### 4.2 Thermal response of the granular packing

Having induced the martensitic transformation in this granular packing at room temperature, we explore its reversion to austenite upon heating to 500 °C in the DSC (Steps $3_I$ and $4_I$ in Figure 1). Figure 7 shows the heat flow signals of two DSC cycles for the granular packing. On the first

cycle, similarly to what was described in the previous section for the granular packing in the shape memory regime as shown in Figure 3, there is a long and significant exothermic relaxation process before the reverse martensitic transformation, probably because of the strain energy released during heating. Additionally, the endothermic signal associated with $A_s$ and $A_f$ is not very clear in this case, perhaps because it is broadened out due to a large number of domains, or because of its convolution with the stress relaxation signals. And yet, the reverse transformation to the tetragonal austenite phase does occur over this cycle, as will be shown shortly.

Upon cooling during the first DSC cycle, the sample shows no additional transformations and remains tetragonal to room temperature. The second DSC cycle in Figure 7 confirms that no additional transformations occur subsequently, either. By comparing the XRD patterns of the granular packing before the first DSC cycle (showing a monoclinic phase) and after the second (showing a tetragonal phase), we confirm that reversion to austenite did indeed occur during the first thermal cycle in the DSC.

## 5  Superelastic Regime: $T > A_f$

### 5.1 Forward and reverse martensitic transformation

Our above findings in the intermediate regime ($M_s < T < A_s$) directly confirm that stress-induced martensitic transformation can occur in granular SMCs, so in the superelastic regime ($T > A_f$) we expect that confined uniaxial compression should lead to reversible martensitic transformation. The present results are those from the $(ZrO_2)_{1-x}$-$(CeO_2)_x$ specimen with $x = 15\%$, for which the as-prepared powders are in the tetragonal phase, featuring a strong (101) tetragonal peak at ~29.96° in the XRD pattern of Figure 8. Compaction converts the loose powders to a granular SMC packing, which is nominally expected to undergo forward and reverse martensitic transformation during loading and unloading (Step $1_{SE}$ and $2_{SE}$ in Figure 1). As a result, no monoclinic phase should be detected in *ex situ* XRD characterization, an expectation that is verified in Figure 8.

### 5.2 Energy dissipation under cyclic loading

In Figure 9 (a) we plot the force-displacement curves of 300 mg of $(ZrO_2)_{0.85}$-$(CeO_2)_{0.15}$ powder under confined cyclic compression from 1 to 25 kN. Since the die has a diameter of 6 mm, this corresponds to a compaction stress ranging from 35 to 880 MPa. In this presentation,

the left-hand portion shows the accumulation of total displacement as the specimen ratchets to shorter lengths through the 10 applied cycles, and the right-hand portion overlays the cycles for better comparison. The latter presentation makes plain the large one-time hysteresis in the first cycle, which is associated with densification of the loose powders into a jammed structure that supports the full load. There is some additional densification on each subsequent cycle, as evidenced by the continuing displacement ratchet. However, what is more interesting is that after a few initial cycles, the force-displacement curve of this granular SMC stabilizes to be highly reproducible. Furthermore, the hysteresis of these curves is very large, as might be expected for superelastic loading involving forward and reverse martensitic transformation.

As a control experiment, in Figure 9(b) we plot the force-displacement curves of 300 mg of fully stabilized zirconia (8 mol% $Y_2O_3$, cubic phase) powders under the same loading conditions. This fully stabilized zirconia, being cubic rather than tetragonal, cannot undergo the martensitic transformation during mechanical cycling, and is regarded as an inert comparison case of similar composition and mechanical properties for the superelastic ceria-containing composition. As shown in Figure 9(b), this material shows a series of load-displacement curves typical of compacting, non-deforming powders, with initial cycles causing some densification and leading to a stiff response without a large hysteresis. Similar behavior is also observed in the granular packings in the shape memory regime and the intermediate regime (after the initial loading).

For granular SMCs in the superelastic regime, energy dissipation in each loading cycle may originate from powder densification, fracture, or friction amongst the particles in addition to forward and reverse martensitic transformations. The energy dissipation caused by the former three mechanisms should decay as the cycle number increases, and the sample gradually exhausts all the granular rearrangements available to it. However, the energy dissipation caused by the reversible phase transformation should be persistent and essentially independent of the number of cycles, even after the granular packing ceases rearranging its configuration. Figure 10 shows the energy dissipation of the granular SMC zirconia-ceria alloy under cyclic compression at a maximum compressive stress of 880 MPa in each cycle. In the first five cycles, the amount of energy dissipation significantly decreases from 4.2 to 2.2 J/g. After that, the amount of energy dissipation is weakly dependent on the cycle number, stabilizing at a value ~2 J/g. To compare, we also plot the energy dissipation density of the control, non-transformable, powders (8%

yttria-stabilized zirconia, cubic phase). In this case, the amount of energy dissipation significantly decreases with loading cycles, decreasing from 2.1 J/g in Cycle 2 to 0.5 J/g in Cycle 10. There is no apparent 'stable' value for energy dissipation up to 15 loading cycles.

These results, taken together, support the view that the SMC granular packing has access to an additional energy dissipation mechanism that the non-transforming, cubic zirconia powders do not. While the control sample can dissipate energy by powder rearrangement, friction, and fracture events, the SMC powders can additionally transform reversibly; presumably, the much higher value of energy dissipated by that sample is due to the transformation. Interestingly, the stable energy dissipation density (~2 J/g) for the SMC packings, which is significantly higher than that obtained from non-transformed powders, is considerably lower than is theoretically possible for the transformation. For example, based on the hysteresis in DSC scans in Figures 3 and 4, the energy dissipation in a thermally-induced transformation cycle is calculated as ~6.5 J/g for loose powders. Similarly, the energy dissipation measured during compression of a micro-pillar of a similar composition is ~8 J/g [6]. The simplest explanation for this mismatch is that the granular packing does not fully transform, and thus the fractional energy dissipated in the granular packing in Figure 9 and 10 is a measure of the transformed volume fraction of each cycle, which we infer to be ~25-30 % for the granular packing with a composition of $(ZrO_2)_{0.85}$-$(CeO_2)_{0.15}$.This inference is supported by recent work of Du *et al.* [28] showing that cyclic compression of a single superelastic particle (16 mol%Ce-$ZrO_2$) also results in energy dissipation, with the stabilized energy density measured as 3.3 J/g. This value is more closely comparable to the characteristic value of ~ 2 J/g observed in the granular packing here. In the discussion that follows we will explore how the geometry of powders leads to only partial transformation.

## 6. Discussion

All of the evidence presented in the above sections conforms to expectations of how a shape memory material should react when compressed as a granular solid, when there is no significant plasticity in the system. Signatures of reversible transformation are seen during cyclic loading in the superelastic regime, while signatures of texture change due to martensite reorientation under stress are observed in the shape memory regime. Direct evidence for the transformation is provided by the experiments in the intermediate regime, where the transformation is stress-triggered and can be directly measured by *ex situ* X-ray diffraction at room temperature.

One feature that is present both in the superelastic and the intermediate regimes is that the forward transformation is incomplete. In the superelastic regime we estimated a transformation of perhaps 25%-30% of the granular packing to martensite based on cyclic energy dissipation, while in the intermediate regime Figure 6 suggests stress-induced transformation of an additional 38% over the initial condition, apparently a saturation value for those experiments.

The saturation limit for the transformed volume in granular SMCs may originate from the non-uniform stress distribution in powder-die compaction. There are significant stress variations in such a packing at many levels, including macroscopic, i.e., between the confining walls and compact center; mesoscopic, i.e. between different particles that are coordinated and oriented differently within the packing, and even microscopic, i.e., within each individual powder particle. Focusing for the moment just on the last of these, we note that, according to contact mechanics [52], when two particles are in contact, the maximum deviatoric stresses (which would drive the transformation) arise in the regions close to the contact point, and the magnitude of shear stress is much lower in the internal region of the particle. As a result, a small region close to the contact points between powder particles would be expected to transform first, while other regions in the particle remain tetragonal and experience only elastic deformation. As the external loading increases, new regions transform to monoclinic, whereas the already transformed monoclinic regions undergo elastic deformation. The limiting factor on the transformation volume may be geometrical in nature, with an emergent backbone of connected monoclinic phase that can shield load from the tetragonal phase, or, more generally, when the monoclinic phase begins to fracture, relieving local stresses rather than facilitating further transformation.

To preliminarily explore the possible distribution of transformed regions, we use finite element simulation of single-particle compression, which may be viewed as a simple unit model of the contact physics that prevail at many particle-particle contacts throughout a granular packing, without addressing the complexity of stress distribution throughout such a packing. The model is not intended to simulate details of the austenite-martensite transformation in SMCs, which is challenging because it is crystallographic, anisotropic, and dependent on the microstructure [49, 53] and stress states [18-19]. Instead, we simply adopt a constitutive behavior that permits strain accumulation at a constant deviatoric-stress such as is seen during a martensitic transformation. This enables us to approach the problem from a perspective of

powder compression mechanics, and, importantly, to approximate the transformed volume that might be achieved on average.

In our model, transformation is triggered when the local equivalent plastic strain ($\int_0^t \sqrt{\frac{2}{3} \dot{\varepsilon}_{ij}^p \dot{\varepsilon}_{ij}^p} dt$ based on von-Mises plasticity [54], where $\varepsilon_{ij}^p$ is the ij-component of plastic strain tensor) is greater than zero, and the transformation accommodates an amount of deviatoric strain at a constant level of the critical stress. Finally, the transformed region can carry higher stresses through deformation of the monoclinic phase, with a sharp linear increase in stress. The input mechanical response is thus summarized by the constitutive behavior illustrated in Figure 11 (a), which consists of an initial linear elastic stage associated with elastic deformation of the tetragonal phase, a plateau associated with martensitic transformation, and a second linear stage associated with deformation of the monoclinic phase.

We have implemented this constitutive behavior in a 2D axisymmetric model of a spherical particle, quasi-statically compressed by a rigid plate. Figure 11(b) illustrates the main features of the model that is built in ABAQUS 6.14-3. Incremental displacement is applied in the *y* direction by the plate, which is constrained in the *x* direction. A mirror-symmetry boundary condition is applied on the *y*-axis equator. The contact between the plate and the particle is considered frictionless. 4-node bilinear quadrilateral elements are used to discretize the particle. We assume that any nodal point with non-zero equivalent plastic strain can be considered as a transformed point, and the transformed volume fraction ($V_T$) is calculated by the ratio of the transformed nodes to the total nodes. Different particle radii (R = 50, 100 and 200 µm) are considered in our simulations. Since our experiments use powder particle sizes that are smaller than a typical grain size for heat treated zirconia, we envision that most powder particles are single crystalline or close to it. We therefore neglect any effects of grain size on the transformation as a starting assumption.

The elastic modulus is taken to be 200 GPa [55, 56] for the tetragonal phase and we assume the same value for the monoclinic phase. The Poisson's ratio is 0.25. We run the models up to a maximum von Mises stress of 3-5 GPa in the monoclinic phase, and require the equivalent von Mises stress ($\sqrt{\frac{3}{2} S_{ij} S_{ij}}$, where $S_{ij}$ is the ij-component of the deviatoric stress tensor) to follow the

behavior shown in Figure 11.     The plateau strain ($\Delta\varepsilon$) is considered to be 8% [6] in all simulations. Since we model only the loading portion of the experiment, the simulations can be applied to both the superelastic and intermediate regimes, in both of which stress-induced martensitic transformation occurs upon loading.  For the intermediate regime, the transformation occurs at lower stress levels. As a result, our simulation considers three different transformation stress levels, $Y = 500$, 750 and 1000 MPa.

  Figure 12 shows ten snapshots taken during the deformation of a powder particle with 50 µm radius and with $Y = 1000$ MPa critical transformation stress upon compression. The left half of each snapshot illustrates the distribution of each phase, tetragonal (T) and monoclinic (M), whereas the right half shows the von Mises stress distribution in the particle. In the early stage, exemplified at 0.5 mN load, the induced stress is not high enough to drive the transformation. However, the stress is concentrated just beneath the contact surface and, as the load increases, the first regions of monoclinic phase appear there, such as shown at 1.6 mN load. With an increase in load, the monoclinic phase grows in all directions and soon reaches the surface. As the external loading increases afterwards, the transformation progresses into a larger volume of the particle with a uniform expansion away from the first contact point. Similar phenomena are observed for the cases of different particle radii (for 100 and 200 µm) and different values of critical transformation stress (for $Y = 500$ and 750 MPa)

  As described above, we can imagine at least two points in the evolution in Figure 12 at which continued transformation might cease:

- First, the formation of a percolating backbone of martensitic phase that shields additional load from austenite might cause the transformation to cease.  In Figure 12 this happens in the last frame, when the martensite traverses the full particle.  Such percolation would likely happen sooner in a granular packing compared to the particle-particle contacts studied here, because of the higher coordination of particles. Moreover, the percolating backbones between neighboring particles would connect together, resulting in the formation of martensite chains along the compression loading direction throughout the whole granular packing.  Even for nontransforming particles under gradual loading conditions, force chains form inside compressed granular packings, with the stresses transmitted along them and avoiding material lying

15

between the force chains, which does not support any load [57-60]. In superelastic granular packings, we suggest that such force chains would be preferentially formed along the transformed martensite phase, which would form into a percolating martensitic backbone that effectively shields load from the untransformed austenite regions between the martensitic force chains and prevents further martensitic transformation. This mechanism is illustrated in the upper right in Figure 13.

- Second, even before the percolating backbone of martensite forms, transformation may stop due to particle fracture. As shown in Figure 12, as the transformed region enlarges, there is a concentration site of stress accumulation near the edge of the contact zone, in the monoclinic phase. This concentration site achieves very high stress levels well before the martensitic phase has percolated through the diameter of the particle. For example, under a 2.24 N compressive load, local stresses up to 4.5 times higher than the transformation stress emerge at this location; such sites may be prone to fracture of the martensite phase, and thus would limit the extent of transformation. We thus envision a critical stress $\sigma_f$ that would be the maximum sustainable stress for the transformed monoclinic phase, beyond which martensitic transformation propagation will stop in SMC particles due to fracture and spontaneous stress relief. This mechanism is illustrated in the lower right in Figure 13. However, we note that the transformed volume is independent of the powder size for given transformation and fracture stresses, so particle fracture and particle size reduction may not account for the transformation plateau unless it leads to particle rearrangements that involve more shielding as described above.

In order to better connect the simulation results to our experiments requires a conversion from the local applied forces in the single-particle model to the average applied compaction pressure in the experiments. For a perfect elastic-plastic material, the relationship between the applied pressure and relative density can be approximated as [61, 62]

$$P_h = 3D^2 \frac{D - D_0}{1 - D_0} \sigma_y \approx 1.3 \frac{D^3 - D_0^{\,3}}{1 - D_0} \sigma_y, \tag{1}$$

for the scenario of hydrostatic compression. Here $P_h$ is the applied hydrostatic pressure, $\sigma_y$ is the yield strength, $D$ is the relative density of the whole packing, and $D_0$ is the initial relative density

before compression. In the context of compression of granular shape memory ceramics, $\sigma_y$ should be interpreted as the critical stress to trigger martensitic transformation rather than the yield strength, as seen in Figure 11 (b), with the transformation plateau providing a convenient analogy to perfectly-plastic behavior. The average contact force between particles of radius $R$ can be modeled as [61, 62] $f = P_h \dfrac{\pi R^2}{3D^2}$, which when introduced into Eq. (1) gives the average contact force as a function of the applied pressure:

$$f(P) = \frac{1+2\alpha}{3} P \frac{\pi R^2}{3} [\frac{(1-D_0)P}{1.3\sigma_y}(\frac{1+2\alpha}{3}) + D_0^{\,3}]^{-2/3}. \qquad (2)$$

Here the quantity $\dfrac{1+2\alpha}{3}$ provides a conversion from uniaxial to hydrostatic pressure with the stress transmission coefficient $\alpha$ [49] being the ratio between radial stress and axial stress, which might reasonably range between 0.5 (for hard particles) and 0.9 (for elastic-plastic ones) [49, 63-65].

Using the same set of parameters in the finite element modeling in Figure 12, i.e. $R = 50\ \mu m$ and $\sigma_y = 1000\ \mathrm{MPa}$, along with a theoretical value of $D_0 = 0.64$ [61], allows us to rescale the force axis in Figure 12 to match the experimental pressure scale of the *ex situ* phase characterization results seen in Figure 6. The result of this comparison is presented in Figure 14, with the analytical modeling generally matching the concave-downward trend in the experimental data. The simulations thus support the most critical experimental observation, namely, that the rate of transformation (i.e. transformation fraction with increasing stress) declines at higher loading levels; there are diminishing returns obtained by loading to ever higher levels. Looking more closely, the experimental data shows a more severe levelling-off and an apparent plateau, but given the many simplifications in the model—the simplified transformation modeling, the contact geometry, the lack of longer-range force chains as in a true granular packing—we find the agreement reasonable as a first approximation. The fact that different parts of the curve match better with different confinement parameters $\alpha$ also seems to suggest a complexity in the evolving stress level as the transformation occurs. It is an interesting direction for future work to develop constitutive laws that can accurately reflect the average compact stress distribution as the particles progressively transform.

## 7. Conclusion

We have conducted a systematic study on the mechanical and thermal responses of granular shape memory ceramics (SMCs) in three different regimes. The most salient results in this work include the following:

- In the shape memory regime ($T < M_f$), confined uniaxial compression leads to martensite re-orientation, in which the randomly textured powders become a granular SMC packing with a preferred crystallographic orientation. The degree of texture increases with the magnitude of the axial stress. This texture is significantly reduced after thermal cycling, due to self-accommodation during thermally-induced martensitic transformation.

- In the intermediate regime ($M_s < T < A$s), stress-induced martensitic transformation is irreversible. Because of the non-uniform stress field, the martensitic transformation readily occurs at a low nominal compressive stress, with the transformed volume increasing with axial stress. *Ex situ* XRD characterization in this regime provides direct evidence of stress-induced martensitic transformation in granular SMC packings.

- In the superelastic regime ($T > A_f$), confined uniaxial compression leads to forward and reverse martensitic transformation during loading and unloading respectively. The energy dissipation density in this process is remarkably high, ~2 J/g when cycling up to a compressive axial stress of 880 MPa.

- Stress-induced martensitic transformation in granular SMC packings is limited by the non-uniform stress distribution in powder-die compaction to a volume fraction on the order of 25-40%. Finite element modeling at the particle level corroborates this observation; even within a single particle the transformation may be incomplete due to the non-uniform contact stress field.

The findings in this work pave the way toward using granular SMCs in bulk applications, e.g. for energy dissipation and cyclic damping. As a final observation, Figure 15 compares the energy dissipation capability of granular SMCs with other shape memory materials [6, 9, 66-70] at different length scales. The high energy dissipation capacity of SMCs can be brought to macroscopic scales through the use of granular packings.

## References
[1]     Miyazaki S, Otsuka K. Isij International 1989;29:353.
[2]     Otsuka K, Ren X. Progress in Materials Science 2005;50:511.
[3]     Otsuka K, Ren XB. Intermetallics 1999;7:511.
[4]     Tadaki T, Otsuka K, Shimizu K. Annual Review of Materials Science 1988;18:25.
[5]     Chluba C, Ge W, de Miranda RL, Strobel J, Kienle L, Quandt E, Wuttig M. Science 2015;348:1004.
[6]     Lai A, Du Z, Gan CL, Schuh CA. Science 2013;341:1505.
[7]     Omori T, Ando K, Okano M, Xu X, Tanaka Y, Ohnuma I, Kainuma R, Ishida K. Science 2011;333:68.
[8]     Tanaka Y, Himuro Y, Kainuma R, Sutou Y, Omori T, Ishida K. Science 2010;327:1488.
[9]     Otsuka K, Wayman CM. Shape memory materials. New York: Cambridge University Press, 1998.
[10]    Bhattacharya K. Microstructure of martensite : why it forms and how it gives rise to the shape-memory effect. Oxford ; New York: Oxford University Press, 2003.
[11]    Lagoudas DC. Shape memory alloys : modeling and engineering applications. New York ; London: Springer, 2008.
[12]    Swain MV. Nature 1986;322:234.

[13]    Heuer AH, Lange FF, Swain MV, Evans AG. Journal of the American Ceramic Society 1986;69:R1.

[14]    Kelly PM, Rose LRF. Progress in Materials Science 2002;47:463.

[15]    Heuer AH, Ruhle M. Acta Metallurgica 1985;33:2101.

[16]    Launey ME, Ritchie RO. Advanced Materials 2009;21:2103.

[17]    Jin X-J. Current Opinion in Solid State & Materials Science 2005;9:313.

[18]    Chen I-W and Reyes Morel PE. Journal of the American Ceramic Society 1986; 69 (3): 181.

[19]    Chen I-W and Reyes Morel PE. Journal of the American Ceramic Society 1986; 69 (3): 189.

[20]    Lovey FC, Torra V. Progress in Materials Science 1999;44:189.

[21]    Sato A, Chishima E, Soma K, Mori T. Acta Metallurgica 1982;30:1177.

[22]    Chevalier J, Gremillard L, Virkar AV, Clarke DR. Journal of the American Ceramic Society 2009;92:1901.

[23]    Hannink RHJ, Kelly PM, Muddle BC. Journal of the American Ceramic Society 2000;83:461.

[24]    Camposilvan E, Anglada M. Journal of the European Ceramic Society 2015;35:4051.

[25]    Du ZH, Zeng XM, Liu Q, Lai A, Amini S, Miserez A, Schuh CA, Gan CL. Scripta Materialia 2015;101:40.

[26]    Xu ZW, Wang MY, Chen TN. Journal of Sound and Vibration 2005;279:1097.

[27]    Wei ZG, Sandstrom R, Miyazaki S. Journal of Materials Science 1998;33:3743.

[28]    Wei ZG, Sandstrom R, Miyazaki S. Journal of Materials Science 1998;33:3763.

[29]    Friend RD, Kinra VK. Journal of Sound and Vibration 2000;233:93.

[30] Du Z, Zeng XM, Liu Q, Schuh CA, Gan CL. Acta Materialia 2017; 123: 255-263.

[31] Van Humbeeck J. Materials Science and Engineering: A 1999; 134

[32] Jani JM, Leary M, Subic A, Gibson MA. Materials & Design 2014; 56:1078.

[33] Fu Y, Du H, Huang W, Zhang S, Hu M. Sensors and Actuators A: Physical 2004; 112:395.

[34]    Krulevitch P, Lee AP, Ramsey PB, Trevino JC, Hamilton J, Northrup MA. Journal of Microelectromechanical Systems 1996;5:270.

[35]    Miyazaki S, Fu YQ, Huang WM, Books24x7 Inc. Thin film shape memory alloys fundamentals and device applications. Cambridge, U.K. ; New York: Cambridge University Press, 2009.

[36]    Barbarino S, Flores EIS, Ajaj RM, Dayyani I, Friswell MI. Smart Materials and Structures 2014;23.

[37]  Carpinteri A, Lacidogna G, Pugno N. International Journal of Fracture 2004;129:131.

[38] Anderson TL. Fracture Mechanics: Fundamentals and applications. CRC Press 1995.

[39] Lai A. Ph.D. thesis. Department of Materials Science and Engineering, Massachusetts Institute of Technology, Cambridge, USA; 2016.

[40] Swain MV, Hannink RHJ, Journal of American Ceramic Society 1989; 72 (8): 1358-1364.

[41] Reyes Morel PE and Chen I-W. Journal of the American Ceramic Society 1988; 71(8): 354.

[42] Reyes Morel PE and Chen I-W. Journal of the American Ceramic Society 1988; 71 (8): 648.

[43] Kabekkodu S. *Powder Diffraction File Inorganic and Organic Data Book, International Center for Diffraction Data* (2010).

[44]    Witherspoon C, Zheng PQ, Chmielus M, Vogel SC, Dunand DC, Mullner P. Acta Materialia 2013;61:2113.

[45]    Cai S, Schaffer JE, Ren Y, Yu C. Applied Physics Letters 2013;103.

[46]    Stebner A, Gao X, Brown DW, Brinson LC. Acta Materialia 2011;59:2841.

[47]    Li B-S, Cherng J-S, Bowman KJ, and Chen I-W. Journal of the American Ceramic Society 1988; 71 (7): C-362.

[48]    Liu Y, Xie ZL, "Detwinning in shape memory alloy", chapter in Progress in smart materials and structures research, Nova science Publishers, Inc. 2006, ISBN 1-60021-106-2.

[49]    Zeng XM, Lai A, Gan CL, Schuh CA. Acta Materialia 2016; 116:124-135.

[50]    Brewin PR. Modelling of powder die compaction. London: Springer, 2008.

[51]    Fleck NA, Kuhn LT, McMeeking RM. Journal of the Mechanics and Physics of Solids 1992;40:1139.

[52]    Johnson KL. Contact mechanics. Cambridge Cambridgeshire ; New York: Cambridge University Press, 1985.

[53]    Camposilvan E, Anglada M. Acta Materialia 2016;103:882.

[54] Boresi AP, Schimidt RJ, Advanced Mechanics of Materials, 6th Edition, John Willy & Sons Inc., 2003.

[55] Eichler J, Eisele U, Rodel J. Journal of the American Ceramic Society 2004;87:1401.

[56]Adams JW, Ruh R, Mazdiyasni KS. Journal of the American Ceramic Society 1997;80:903.

[57] Hidalgo RC, Grosse CU, Kun F., Reindardt HW. Herrmann HJ. Physical Review Letters 2002; 89: 205501.

[58] Majmudar TS and Behringer RP. Nature 2000; 435: 7405.

[59] Behringer RP et al., Phil. Trans. R. Soc. A 2008; 366, 493–504

[60] Liu, A. J. & Nagel, S. R. Nature 1998*;* 396, 21–22.

[61] Fischmeister HF, Arzt E. Powder Metallurge 1983; 26:82

[62] Helle AS,  Easterling KE,  Ashby MF. Acta Metall. 1985; 33: 2163.

[63] Long WM. Powder Metallurgy, 1960; 6: 73.

[64] Bockstiegel G. and Hewing J. 2nd European Symposium on Powder Metallurgy, Stuttgart, 1968.

[65]   DiMilia, R. A. and Reed, J. S., Am. Ceram. Soc. Bull., 1983; 62: 484.

[66]    Chen Y, Schuh CA. Acta Materialia 2011;59:537.

[67]    San Juan J, No ML, Schuh CA. Advanced Materials 2008;20:272.

[68]    San Juan J, No ML, Schuh CA. Nature Nanotechnology 2009;4:415.

[69]    Chen Y, Zhang X, Dunand DC, Schuh CA. Applied Physics Letters 2009;95.

[70]    Dunand DC, Muellner P. Advanced Materials 2011;23:216.

**Figure captions**
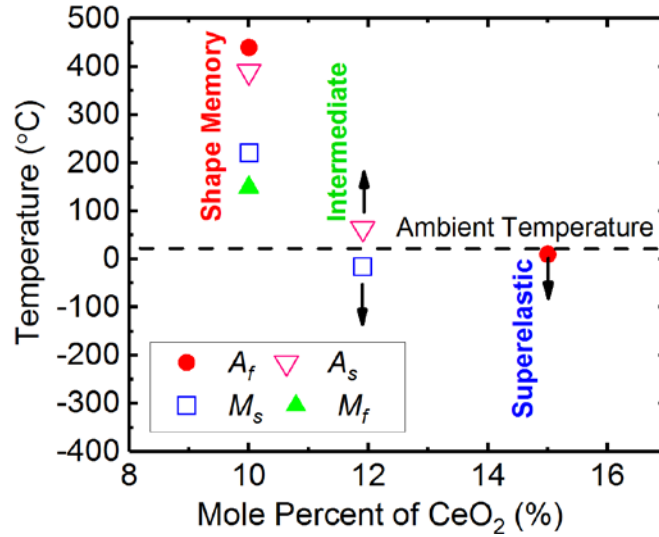
Figure 1. (a) Stress-temperature diagram for SMCs. Arrows in different colors are used to illustrate experimental steps in the shape memory, intermediate, and superelastic regimes. (b) Transformation temperatures plotted for each of the shape memory, intermediate, and superelastic regimes investigated in this work.
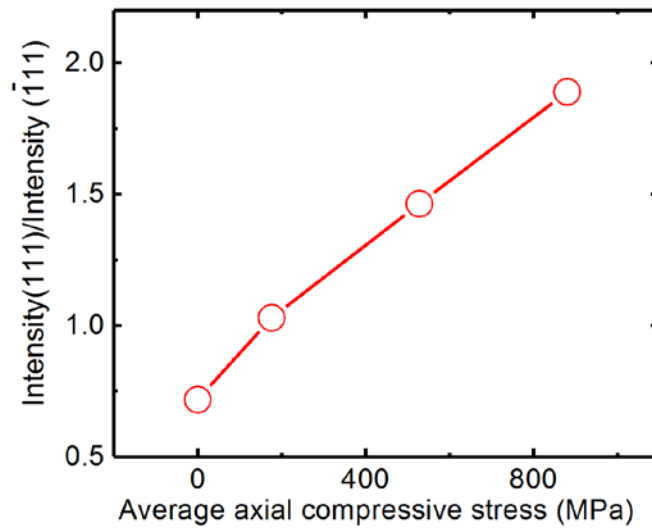
Figure 2. (a) Shape memory regime: XRD two-theta scan pattern of granular $(ZrO_2)_{0.9}$-$(CeO_2)_{0.1}$ before and after confined uniaxial compression at 880 MPa. $M$ stands for monoclinic. (b) Plot of the ratio of monoclinic (111) to ($\bar{1}$11) peak intensity as a function of average axial compressive stress.
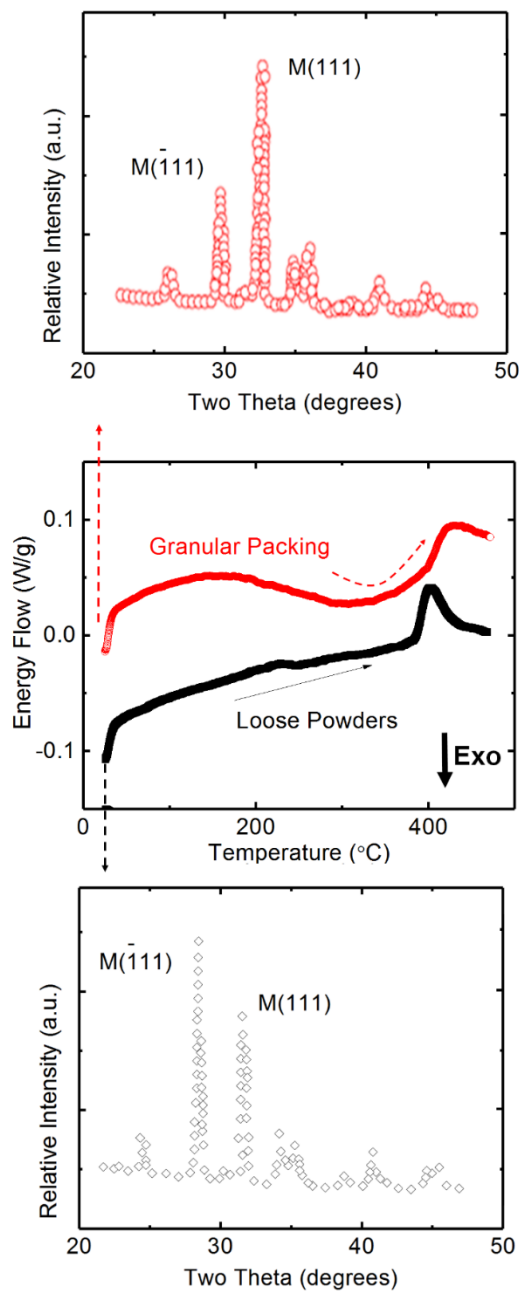
Figure 3. Center figure: differential scanning calorimetry (DSC) curves of the granular packing and loose powders of $(ZrO_2)_{0.9}$-$(CeO_2)_{0.1}$ during heating from room temperature to 500 ºC. Upper and lower figures compare the XRD patterns of the packing and loose powders before the DSC test, with a significant texture seen in the former.

Figure 4. Center figure: differential scanning calorimetry (DSC) curves of the granular packing and loose powders of $(ZrO_2)_{0.9}$-$(CeO_2)_{0.1}$ during cooling from 500 ºC to room temperature. Upper and lower figures show the XRD patterns of the packing and loose powders after the DSC test, suggesting a significant loss of texture after thermally-induced reverse and forward martensitic transformation in the former.

Figure 5. Direct XRD evidence for stress-induced martensitic transformation in the intermediate regime. $T$ and $M$ stand for tetragonal and monoclinic, respectively.

Figure 6. The volume fraction of the monoclinic phase as a function of the axial stress in granular $(ZrO_2)_{0.88}$-$(CeO_2)_{0.12}$ alloy.

Figure 7. Thermal and phase signals of the granular packing of $(ZrO_2)_{0.88}$-$(CeO_2)_{0.12}$ alloy. Two cycles of differential scanning calorimetry (DSC) curves are shown for heating and cooling. The XRD patterns show that the packing is mostly of monoclinic phase before the 1st DSC cycle, but completely transforms to tetragonal phase after the 2nd DSC cycle.

Figure 8. Superelastic regime: XRD pattern of the granular packing of $(ZrO_2)_{0.85}$-$(CeO_2)_{0.15}$ before and after confined uniaxial compression at 880 MPa.

Figure 9. (a) Load-displacement curves of (a) 300 mg $(ZrO_2)_{0.85}$-$(CeO_2)_{0.15}$ powders (tetragonal phase) and (b) 300 mg fully stabilized zirconia powders (cubic phase) under cyclic loading from 35 MPa to 880 MPa. The hysteresis of each cycle is compared on the right by translating all the curves to the same origin.

Figure 10. Plot of energy dissipation density as a function of cycle number: a comparison between the superelastic particles and the non-transformed particles.

Figure 11. (a) Constitute behavior of SMCs used in the model. (b) Details of the finite element model of the powder compression.

Figure 12. Stress distribution and regions of tetragonal and monoclinic phases as load increases in compression of a powder particle with 50 µm radius and with 1000 MPa critical stress. The left and the right quarter in each snapshot illustrate the regions of each phase and stress distribution respectively. $T$ and $M$ stand for tetragonal and monoclinic.

Figure 13. Two-particle loading diagram showing possible origins of the limit of martensitic transformation.

Figure 14. Modeling results of the transformed volume fraction $V_T$ at a given average axial stress $P$, which are compared with the experiments.

Figure 15. Energy dissipation capability of shape memory metals and ceramics at different length scales.

(a)
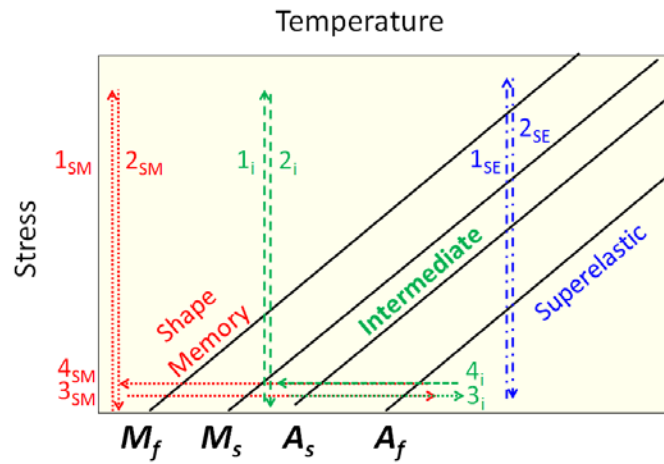


(b)



Figure 1

Figure 1. (a) Stress-temperature diagram for SMCs. Arrows in different colors are used to illustrate experimental steps in the shape memory, intermediate, and superelastic regimes. (b)

Transformation temperatures plotted for each of the shape memory, intermediate, and superelastic regimes investigated in this work.

(a)
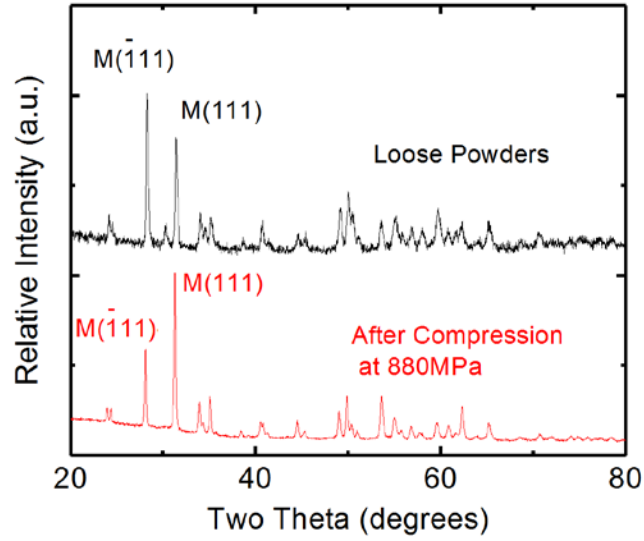


(b)



Figure 2

Figure 2. (a) Shape memory regime: XRD two-theta scan pattern of granular $(ZrO_2)_{0.9}$-$(CeO_2)_{0.1}$ before and after confined uniaxial compression at 880 MPa. $M$ stands for monoclinic. (b) Plot of

the ratio of monoclinic (111) to ($\bar{1}$11) peak intensity as a function of average axial compressive stress.



Figure 3

Figure 3. Center figure: differential scanning calorimetry (DSC) curves of the granular packing and loose powders of $(ZrO_2)_{0.9}-(CeO_2)_{0.1}$ during heating from room temperature to 500 ºC. Upper and lower figures compare the XRD patterns of the packing and loose powders before the DSC test, with a significant texture seen in the former.
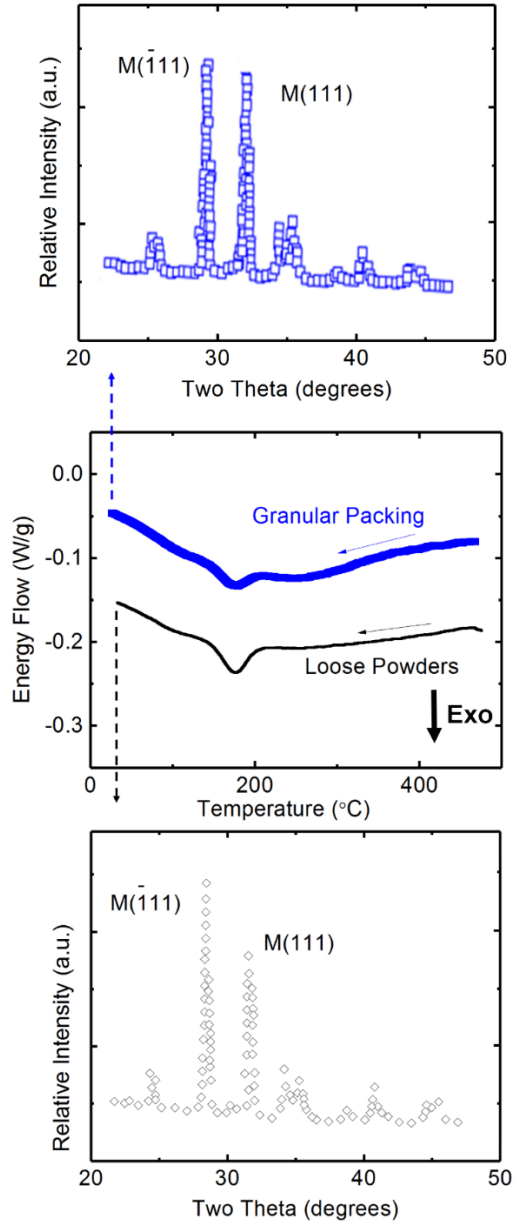


Figure 4

Figure 4. Center figure: differential scanning calorimetry (DSC) curves of the granular packing and loose powders of $(ZrO_2)_{0.9}$-$(CeO_2)_{0.1}$ during cooling from 500 ºC to room temperature. Upper and lower figures show the XRD patterns of the packing and loose powders after the DSC test, suggesting a significant loss of texture after thermally-induced reverse and forward martensitic transformation in the former.
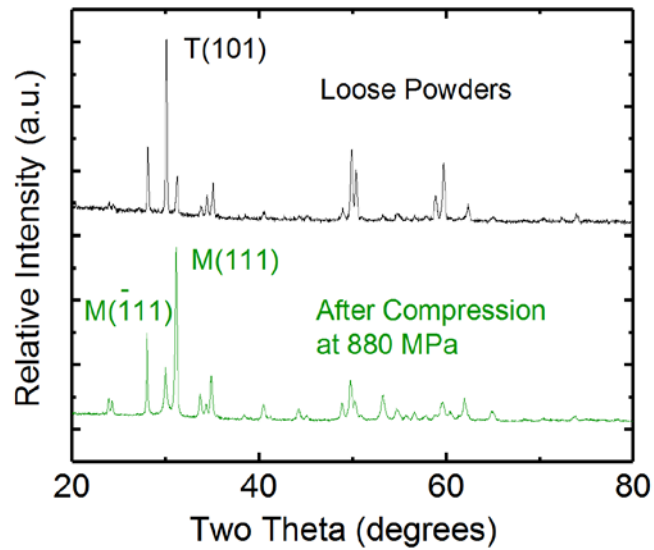


Figure 5.

Figure 5. Direct XRD evidence for stress-induced martensitic transformation in the intermediate regime. *T* and *M* stand for tetragonal and monoclinic, respectively.
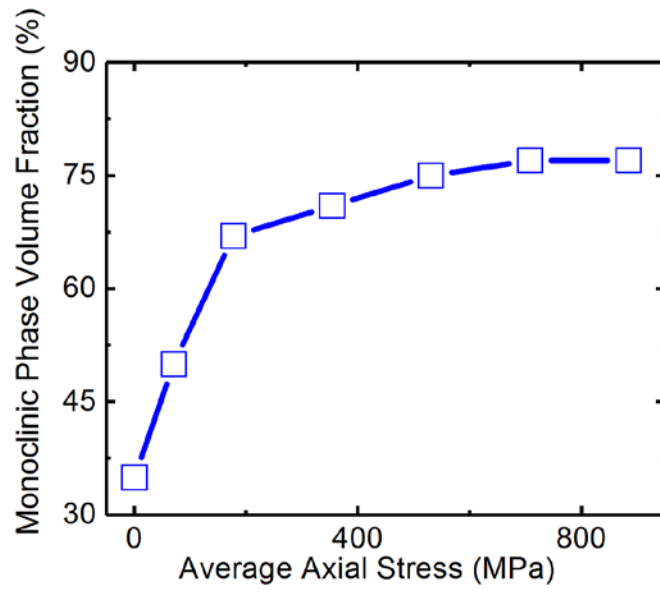
Figure 6**.**

Figure 6. The volume fraction of the monoclinic phase as a function of the axial stress in granular $(ZrO_2)_{0.88}$-$(CeO_2)_{0.12}$ alloy.
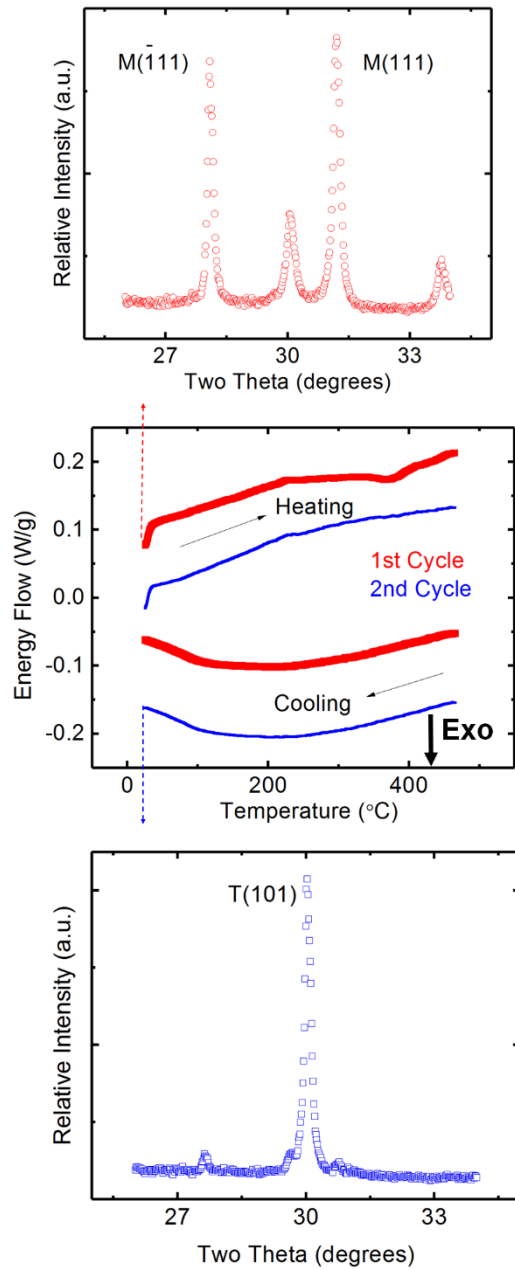
Figure 7

Figure 7. Thermal and phase signals of the granular packing of $(ZrO_2)_{0.88}$-$(CeO_2)_{0.12}$ alloy. Two cycles of differential scanning calorimetry (DSC) curves are shown for heating and cooling. The

XRD patterns show that the packing is mostly of monoclinic phase before the 1st DSC cycle, but completely transforms to tetragonal phase after the 2nd DSC cycle.
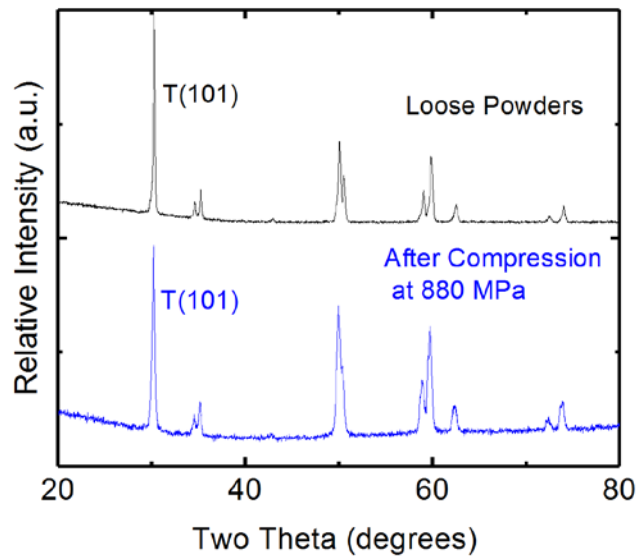


Figure 8.

Figure 8. Superelastic regime: XRD pattern of the granular packing of $(ZrO_2)_{0.85}$-$(CeO_2)_{0.15}$ before and after confined uniaxial compression at 880 MPa.

(a)
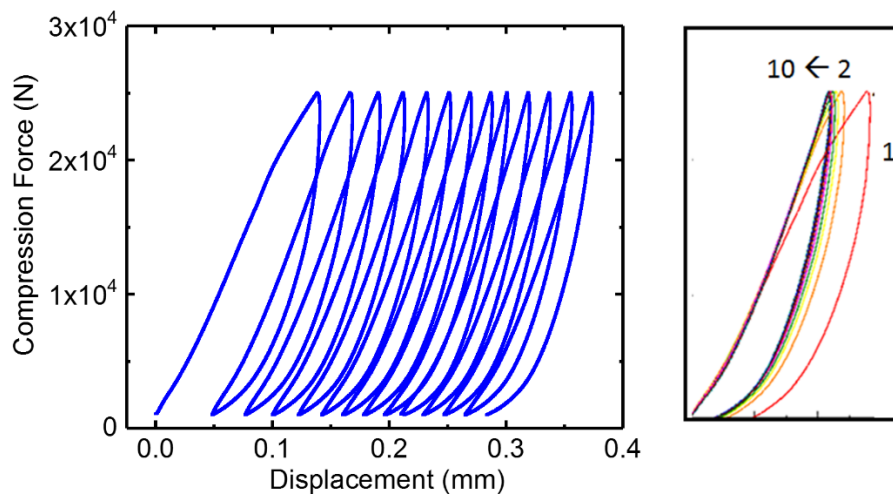


(b)
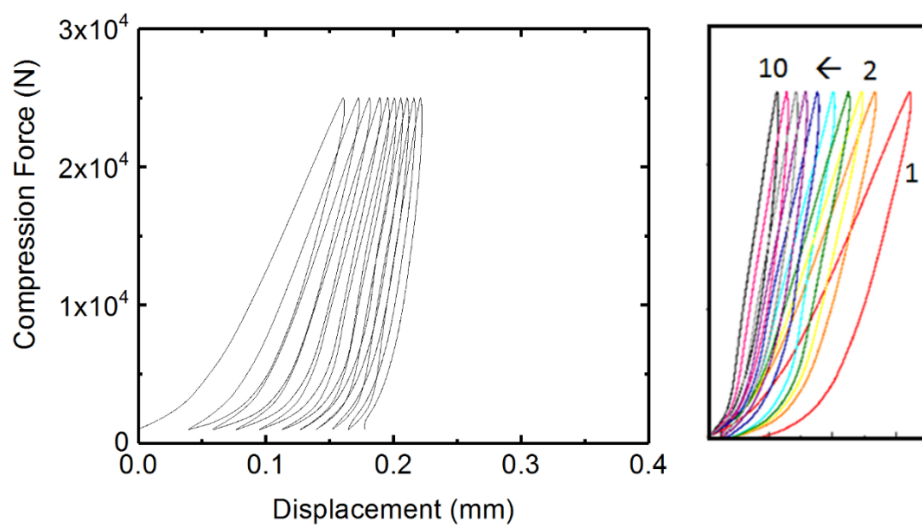


Figure 9

Figure 9. (a) Load-displacement curves of (a) 300 mg $(ZrO_2)_{0.85}$-$(CeO_2)_{0.15}$ powders (tetragonal phase) and (b) 300 mg fully stabilized zirconia powders (cubic phase) under cyclic loading from

35 MPa to 880 MPa. The hysteresis of each cycle is compared on the right by translating all the curves to the same origin.
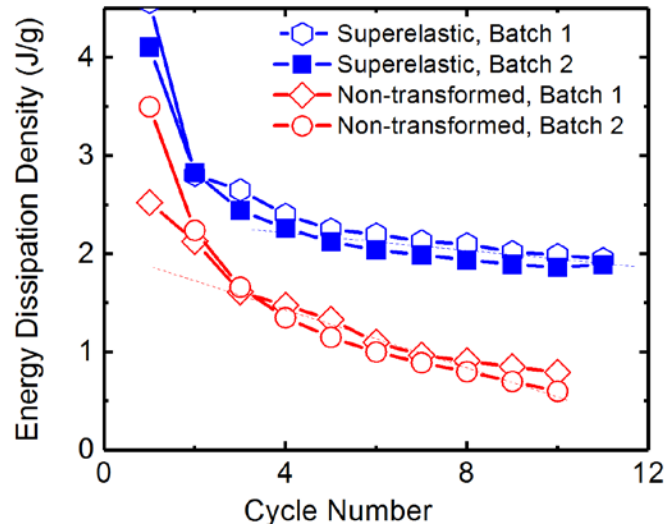


Figure 10

Figure 10. Plot of energy dissipation density as a function of cycle number: a comparison between the superelastic particles and the non-transformed particles.

(a)



(b)



34
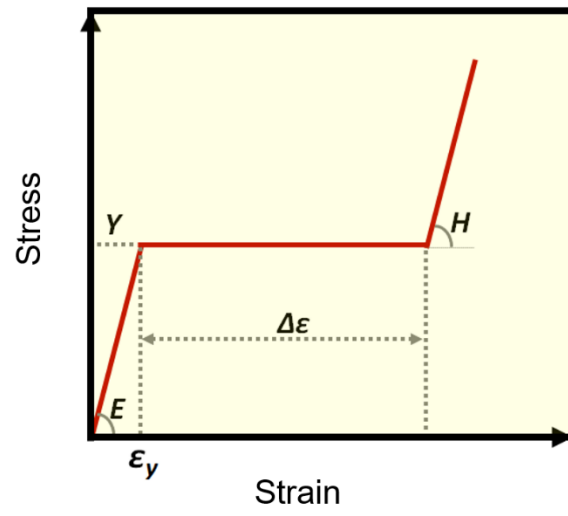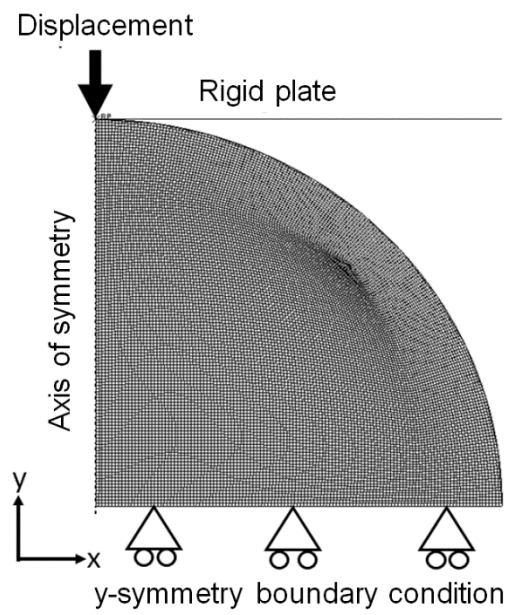
Figure 11

Figure 11. (a) Constitute behavior of SMCs used in the model. (b) Details of the finite element model of the powder compression.
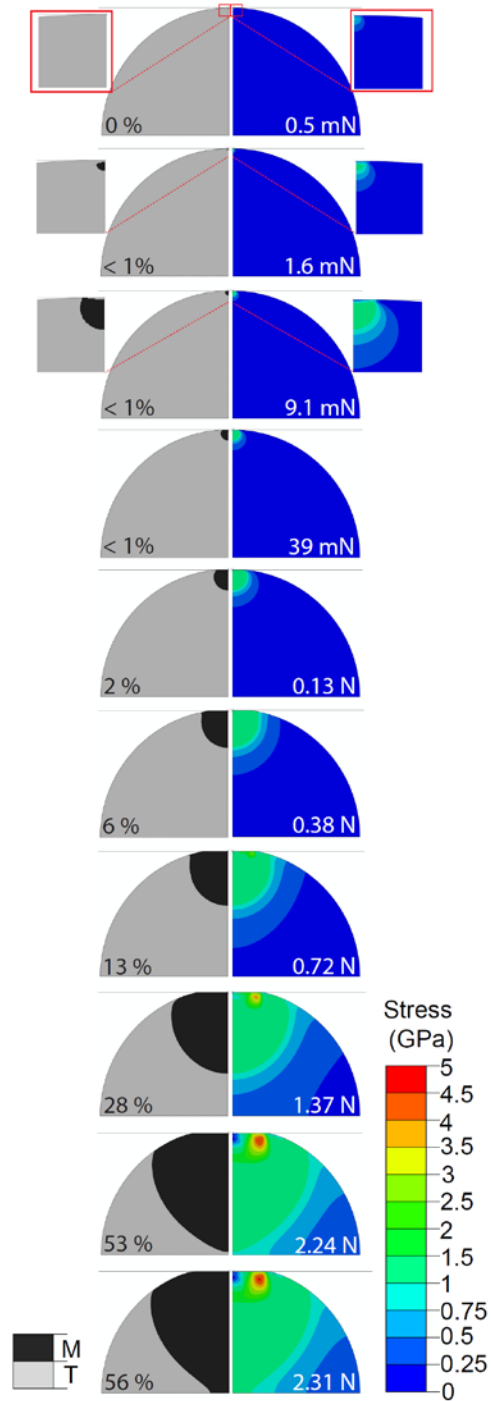
Figure 12

Figure 12. Stress distribution and regions of tetragonal and monoclinic phases as load increases in compression of a powder particle with 50 µm radius and with 1000 MPa critical stress. The left and the right quarter in each snapshot illustrate the regions of each phase and stress distribution respectively. *T* and *M* stand for tetragonal and monoclinic.
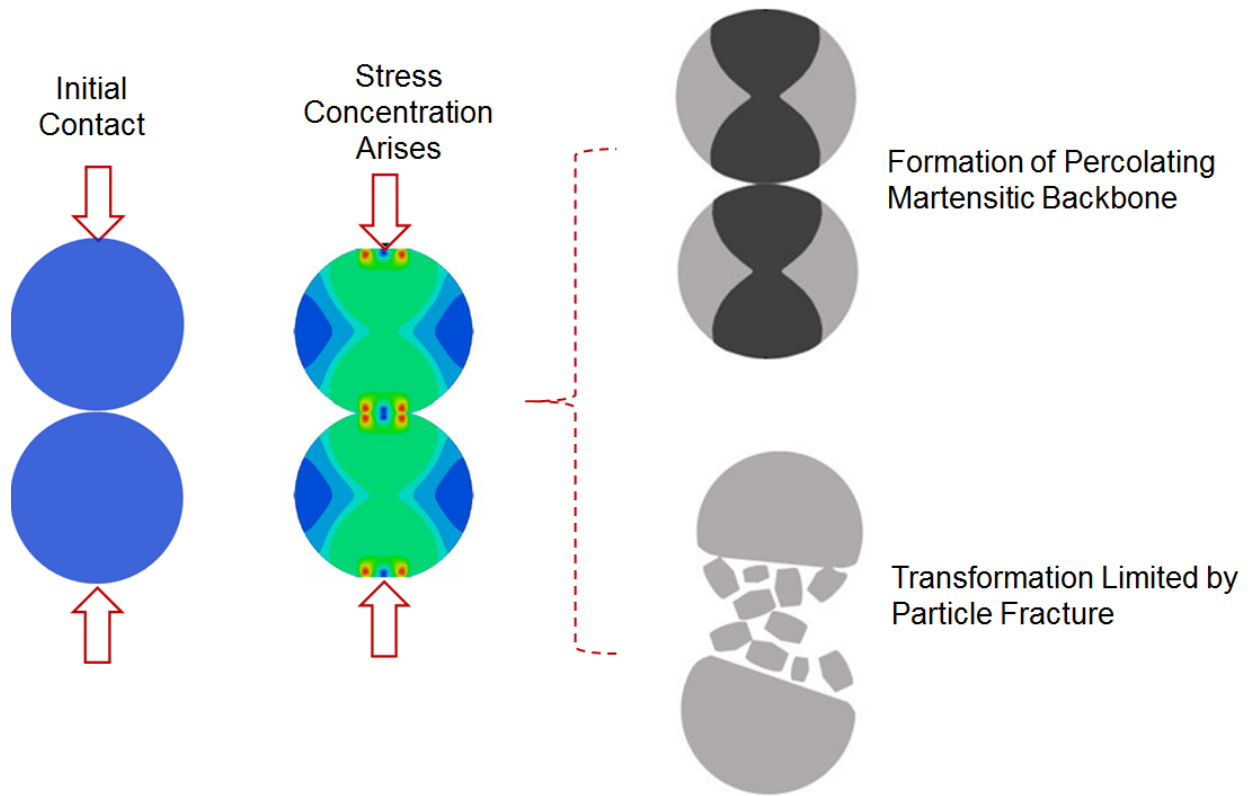


Figure 13

Figure 13. Two-particle loading diagram showing possible origins of the limit of martensitic transformation.
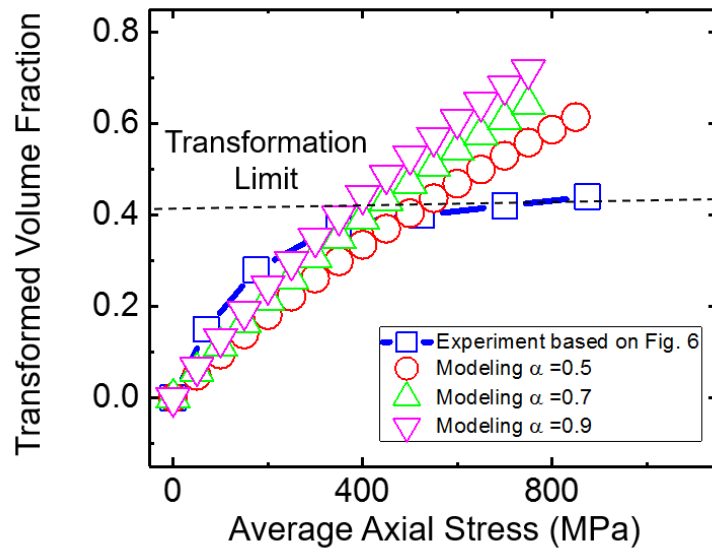
Figure 14

Figure 14. Modeling results of the transformed volume fraction $V_T$ at a given average axial stress $P$, which are compared with the experiments.
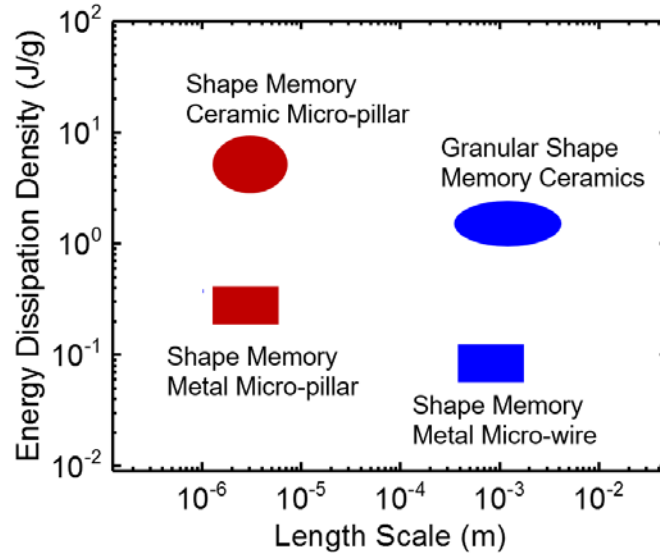
Figure 15

Figure 15. Energy dissipation capability of shape memory metals and ceramics at different length scales.